Front. Earth Sci. 2016, 10(3): 560–569
DOI 10.1007/s11707-016-0583-2

RESEARCH ARTICLE

A new insight into the nature of seasonal variations in coordinate time series of GPS sites located near active faults

Sergey V. TROFIMENKO[1,2], Victor G. BYKOV (✉)[1], Nikolay V. SHESTAKOV[3,4], Nikolay N. GRIB[2], Hiroaki TAKAHASHI[5]

1 Institute of Tectonics and Geophysics, Far Eastern Branch, Russian Academy of Sciences, Khabarovsk 680000, Russia
2 North-Eastern Federal University, Neryungri 678960, the Republic of Sakha (Yakutia), Russia
3 Institute for Applied Mathematics, Far Eastern Branch, Russian Academy of Sciences, Vladivostok 690041, Russia
4 Far Eastern Federal University, Vladivostok 690041, Russia
5 Institute of Seismology and Volcanology, Graduate School of Science, Hokkaido University, Sapporo 060-0810, Japan

Abstract This study provides new insights into the nature of seasonal variations in coordinate time series of GPS sites located near active faults and methods of their modeling. Monthly averaged coordinate time series were analyzed for several pairs of collocated GPS sites situated near the active fault intersection area, in close proximity to the central part of the northern boundary of the Amurian plate and the vicinity of the San Andreas Fault zone. It is concluded that the observed seasonal variations are best described by a breather function which is one of the solutions of the well-known sine-Gordon equation. The obtained results suggest that, in this case, the source of seasonal variations may be caused by the appearance of solitary strain waves in the fault intersection system, which may be qualitatively treated as standing waves of compression-extension of the geological medium. Based on statistical testing, the limits of applicability of the suggested model have been established.

Keywords space geodetic surveys, oscillatory movements of crustal blocks, seasonal variations, Amurian microplate

1 Introduction

The study of seasonal variations of GPS site positions is important to better understand the various-scale natural processes that cause them. These variations reflect the integral impact of many contributing factors (Chen et al., 2013). As a rule, the annual and semiannual modes of seasonal signals are considered, and the sinusoidal-co-sinusoidal approximation is used to model the fluctuations. However, the contemporary precision of GNSS observations allows for a more complicated analysis and time series modeling by applying trigonometric functions with variable amplitude and phase (Chen et al., 2013).

When determining the co- and postseismic displacements and secular crustal movements, the observed seasonal variations are commonly treated as colored noise, masking the useful signal, and are removed during GPS time series preprocessing. Several authors (e.g., van Dam et al., 1994; Serpelloni et al., 2013) have developed models that describe rather well the trajectory of the site movement in the annual and semiannual cycles under the impact of meteorological and hydrological factors. The regional and, more explicitly, global scale parameters of seasonal variations (maxima and minima, duration and power of influence on the geological medium) for collocated sites should coincide due to the identification factors that cause them (temperature, pressure, and gravity variations).

In this paper, we attempt to show that, in a number of cases, the seasonal coordinate variations of GPS sites close to the local active faults exhibit a significant phase shift which cannot be explained by the aforementioned causes. This is validated by the dataset analysis of long-term geodetic observations performed at two different GPS networks, located near the San Andreas Fault zone and the northern boundary of the Amurian plate. Moreover, these GPS site position time series are considerably better described by one of the solutions of the sine-Gordon equation, a breather (spatially localized, oscillating nonlinear function), rather than a sinusoid, as shown in Section 3 below. The experimental data and the developed model of crustal block movement suggest that long-period

Received September 11, 2015; accepted January 20, 2016

E-mail: bykov@itig.as.khb.ru

oscillations of crustal blocks, initiated, for example, by stress variations in the crust or tectonic stress transfer (migrating of crustal deformation in the form of slow strain waves), may be the source of such variations.

2 GPS observations and the extraction of seasonal signals from GPS time series

In order to perform the analysis, we selected a few pairs of GPS sites collocated within 2–30 km in geodynamically active regions near active differently oriented, intersecting faults. Stations NRGR and NRG2 are situated close to the central part of the Stanovoy Range, along the supposed northern boundary of the Amurian plate (Fig. 1(a)). Stations TWMS (33.9725° N, 117.7255° W, City Chino Hills) and CNPP (33.8576° N, 117.6089° W, City Corona), FZHS (34.8680° N, 118.8933° W, City Frazier Mountain) and LJRN (34.8075° N, 118.88677° W, City Frazier Park), accordingly, are located in the San Andreas Fault zone (Figs. 1(b) and 1(c)). The station selection strategy was based on their locations on sides of differently oriented faults.

The daily GPS data of stations NRGR and NRG2 are processed by the GAMIT software (Herring et al., 2010). The site position time series are obtained in the ITRF2005 coordinate system (Altamimi et al., 2007).

Stations TWMS, CNPP, FZHS, and LJRN belong to the GPS network designed to monitor recent crustal movements in the southern part of the San Andreas Fault zone. The GPS network data are processed using the GAMIT/GLOBK software. The daily site position time series are given in the ITRF2005 coordinate system and are available at the SOPAC website (ftp://sopac-ftp.ucsd.edu/pub/time-series/measures/ats/ WesternNorthAmerica/).

To reduce the impact of different short period factors, the monthly averaged site positions are used for further analysis. Collocation of stations in the selected pairs of GPS sites allows for the assumption that seasonal variations in atmospheric parameters are similarly affected (van Dam et al., 1994).

We model the GPS site position time series using the following additive functional model (Serpelloni et al., 2013):

$$x(t) = x_0 + bt + aF(\omega t + \varphi) + \sum_{j=1}^{n} \Delta x_j H(t - t_j), \quad (1)$$

where x is the site position at the moment t along one of the spatial coordinate components, x_0 is the initial station position, b is the secular (annual) velocity, a, ω, and φ denote the amplitude, frequency and initial phase of the seasonal signals, and H is the Heaviside step function, commonly used to determine the displacement of the site Δx_j at appropriate epochs t_j. The first two summands allow for a long-term linear drift of the site determined from its tectonic position. The term $F(\omega t + \varphi)$, as a rule, is a sinusoidal function $\sin(\omega t + \varphi)$, where $\omega = 2\pi/T$, and T is the period of surface loading in the site vicinity. A linear trend and abrupt changes in the site coordinates of different origin are estimated and subtracted from the initial time series values to obtain the pure seasonal variations.

The ITRF2005 position time series of the sites TWMS, CNPP, FZHS, and LJRN are taken from a file, in which the "steps" and linear trends have already been removed (file "WNAM_Clean_DetrendNeuTimeSeries_comb_2014 1114.tar"). No significant seismic events occurred near the sites NRGR and NRG2 before and during the GPS measurements. According to the model results (Shestakov et al., 2012), the displacements from the March, 11, 2011, M_w= 9.0 Tohoku-Oki megathrust earthquake do not exceed 1 mm at this location. It follows that one may neglect the influence of the fourth term on the seasonal variations.

Figures 2 and 3 show the site coordinate time series. The southward station displacement during the winter season is consistent with the general tendency of the GPS site displacement in the Northern Hemisphere (Blewitt et al., 2001). The annual harmonics of the N–S component are represented by nearly identical curves; however, the maximum northward displacement at the NRG2 site is reached in May, whereas it occurs in July at the NRGR site. A similar pattern is exhibited at other sites, affirmed by a two-month delay in the maximum northward displacement at the CNPP site relative to the TWMS site (Figs. 2(c) and 2(d)), with a one- to two-month delay at the LJRN site relative to the FZHS site (Figs. 2(e), 2(f), 3(e) and 3(f)), respectively. The E–W components of the NRGR and NRG2, and TWMS and CNPP sites, respectively, change in an antiphase manner (Figs. 1(a) and 1(b)). A more complicated pattern of the LJRN site movement (Fig. 1(c)) is caused by the presence of the semiannual harmonic.

In order to verify the quantitative differences distinguished in the curve maxima (minima) locations for the aforementioned pairs of sites, we calculate the correlation coefficients for separate components. Let us illustrate our procedure and give an overview of the calculation results. For the pair of sites NRGR and NRG2, we obtain the following correlation coefficient values calculated from 12 monthly averaged values for January–December: $k_{NS}(\Delta\varphi = 0) = 0.43$ for the N–S component and $k_{EW}(\Delta\varphi = 0) = -0.6$ for the E–W component, where $\Delta\varphi$ is the phase shift (in months) between the considered series of values. When shifting a series of values of the N–S component for the NRG2 site to November (by $\Delta\varphi = 2$ months), and those of the E–W component to July (by $\Delta\varphi = 6$ months), the correlation coefficient values are found to be $k_{NS}(\Delta\varphi = 2) = 0.92$ and $k_{EW}(\Delta\varphi = 6) = 0.94$. For the next pair of sites TWMS and CNPP, these calculated values are as follows: $k_{NS}(\Delta\varphi = 0) = 0.41$, $k_{NS}(\Delta\varphi = 2) = 0.99$, $k_{EW}(\Delta\varphi = 0) = 0.37$, and $k_{EW}(\Delta\varphi = 4) = 0.74$, whereas for the vertical component, this value is $k_{Up}(\Delta\varphi = 0) =$

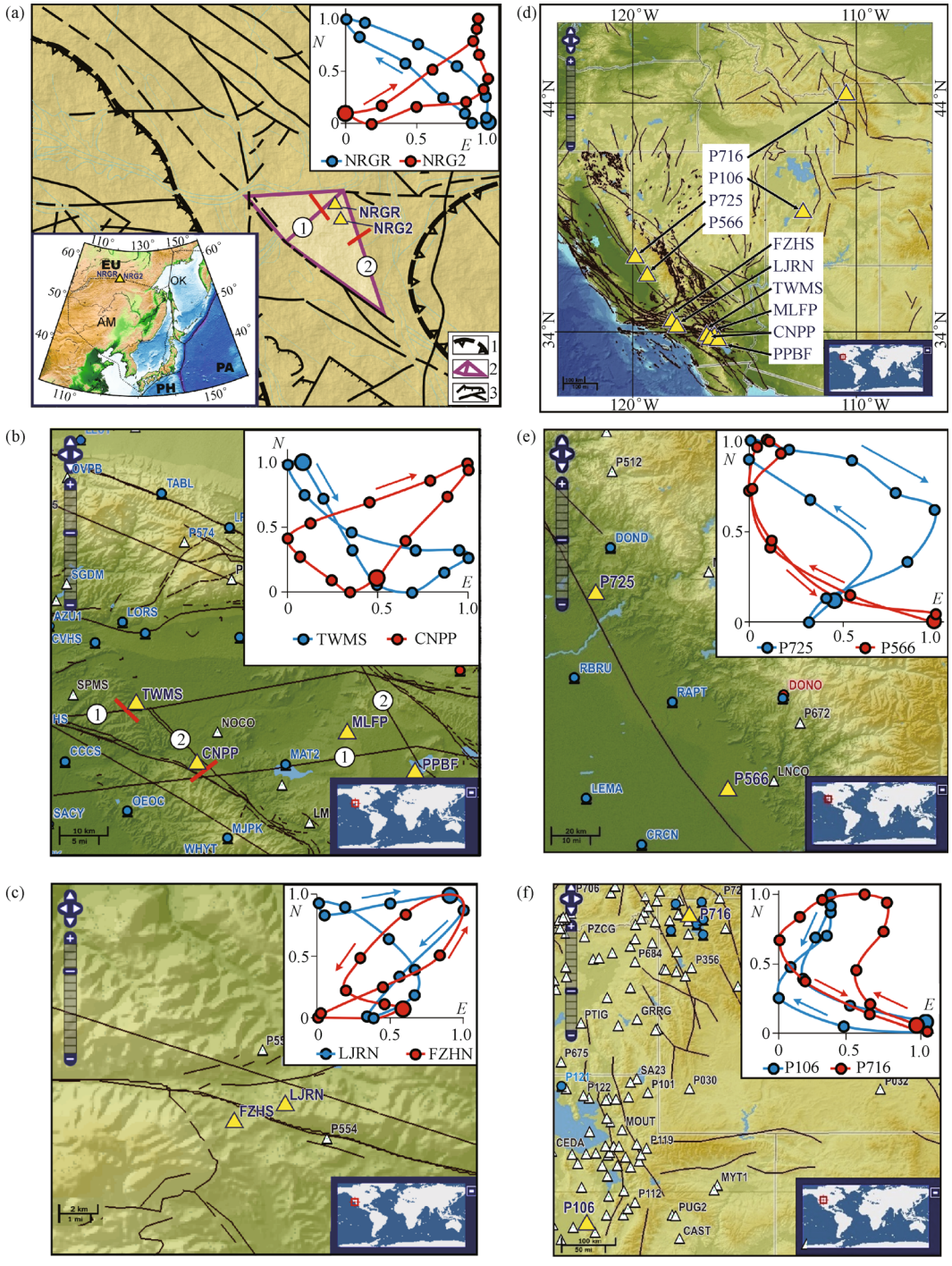

Fig. 1 Schemes of GPS site locations in geodynamically active regions of the world near the intersection of active differently oriented faults. Yellow triangles show GPS site locations. The red lines in insets (a) and (b) indicate the predominant direction of displacement; lines across the faults denote the direction of site displacements in the annual cycles.The insets demonstrate the direction of site movement: a large circle denotes the time reference point (January); the arrows denote the direction of movement. The displacement amplitude is shown in relative value units.Inset (a) depicts GPS sites NRGR and NRG2 at the northern boundary of the Amurian plate: 1 – the boundaries of the Chulman block; 2 – local block bordered by active faults; 3 – NE- and NW-striking faults of different kinematics.Inset at the top: Horizontal displacements of GPS sites. Figures in the circles show: 1 – NE-striking faults, 2 – NW-striking faults. Here and in insets (b)–(f), only horizontal displacements of the sites are shown. Inset at the bottom: Tectonic sketch-map of Northeast Asia: Eurasian (EU), North American (NA), Pacific (PA), Philippine (PH), Amurian (AM), and Okhotsk (OK) plates.Insets (b) and (c) illustrate GPS sites TWMS and CNPP, and FZHS and LJRN, respectively, located in the San Andreas Fault zone and their horizontal displacement trajectories. Figures in the circles show: 1 – NE-striking faults, 2 – NW-striking faults. Inset (d) demonstrates an overview map showing GPS site locations (GPS Explorer Portal; URL: http://geoapp03.ucsd.edu/gridsphere/ gridsphere?cid = Select + Sites). Insets (e) and (f) show GPS sites P725 and P566, and P106 and P716, respectively, relative to the local faults of the system and their horizontal displacement trajectories.

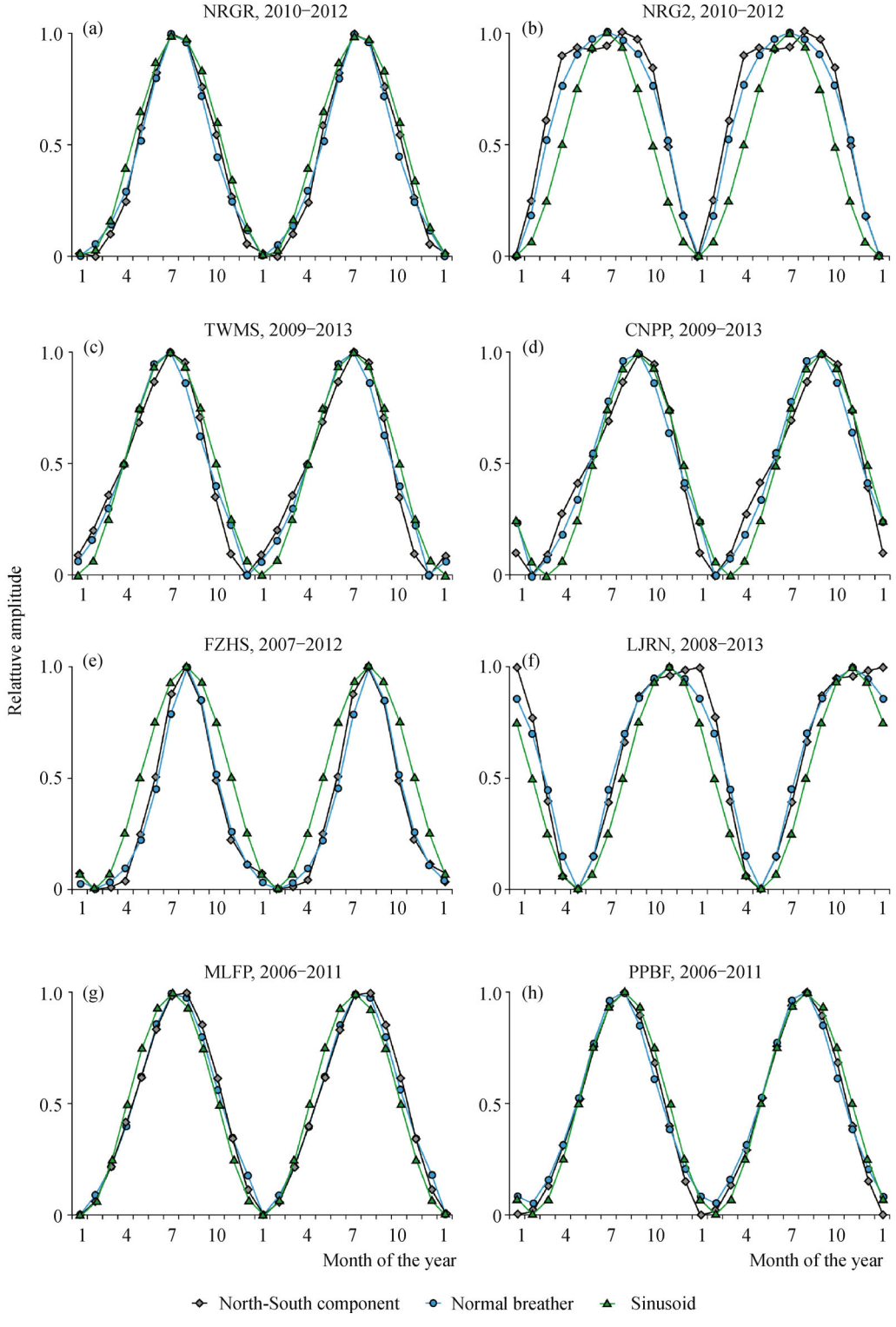

Fig. 2 Cyclic variations in the GPS station positions. Approximation of the generalized normalized average monthly displacement trajectories of the GPS sites by the shape of the theoretical curves for the normal breather and sinusoid. The annual displacements observed during 2 cycles (years) are shown for the N–S components: sites (a) NRGR, (b) NRG2, (c) TWMS, (d) CNPP, (e) FZHS, (f) LJRN, (g) MLFP, and (h) PPBF. The observation periods in years are shown above the plots for each station.

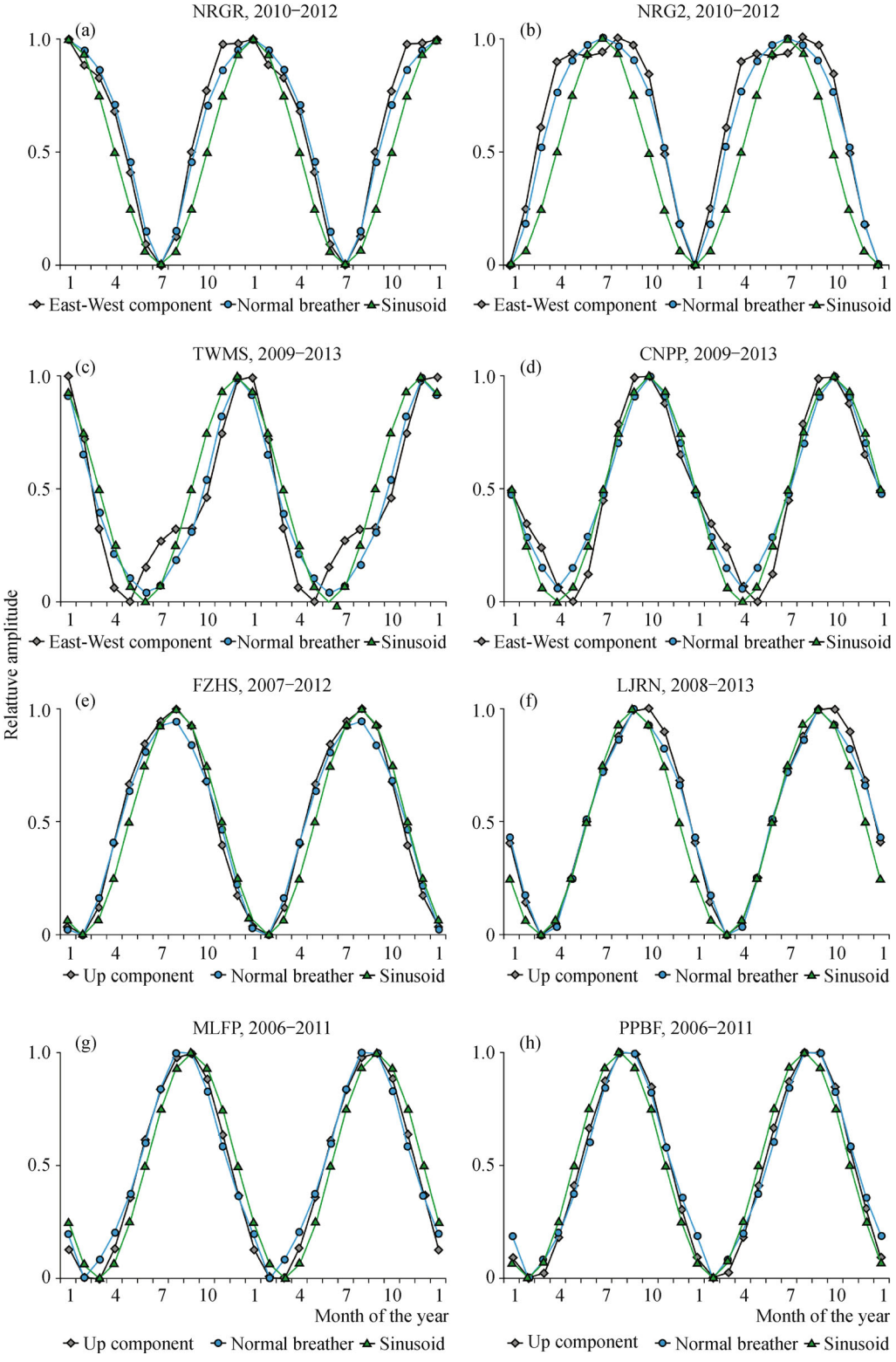

Fig. 3 Cyclic variations in the GPS station positions. Same as Fig. 2, but for the E–W components: sites (a) NRGR, (b) NRG2, (c) TWMS, and (d) CNPP, and for the vertical (Up–Down) component: sites (e) FZHS, (f) LJRN, (g) MLFP, and (h) PPBF.

$k_{Up}(\Delta\varphi = 1) = 0.9$. The correlation coefficient has the following values for the last pair of sites LJRN and FZHS: $k_{NS}(\Delta\varphi = 0) = 0.04$, $k_{NS}(\Delta\varphi = 3) = 0.78$, $k_{EW}(\Delta\varphi = 0) = 0.32$, and $k_{EW}(\Delta\varphi = 3) = -0.84$, respectively; for the vertical component we obtain $k_{Up}(\Delta\varphi = 0) = 0.58$ and $k_{Up}(\Delta\varphi = 3) = 0.99$. In the final analysis, it can be seen that the time shifts between the maxima (minima) of the trajectories of the full displacement vector components have been distinguished for the pairs of sites considered in this study.

Since the GPS sites are collocated (2 km separation between stations NRGR and NRG2, and 30 km between the sites TWMS and CNPP, respectively), their geodetic monuments are proportionately affected by seasonal deformations due to temperature and pressure effects. Thus, the observed seasonal coordinate variations for selected pairs of GPS sites cannot be explained by classical causes. We consider periodic displacements along the faults in close proximity to the GPS sites to be the source of the obtained seasonal variations. The faults, in this case, are playing a hinge role. The local northeast- and northwest-striking faults are hinges for the sites NRGR and TWMS, and NRG2 and CNPP, respectively.

3 Approximation of the initial displacement curves by the functions of different types

We approximate monthly averaged data on the movement trajectories of the GPS sites by a sinusoidal curve $A\sin(\omega t + \varphi)$, minimizing the residuals between the theoretical curve and experimental data using the least squares method. The approximation procedure testifies that separate components of GPS station position displacement are different from the sinusoid (Figs. 2(b), 2(e), and 3(b)).

At the stage of numerical modeling, we clarify that the shape of the best fit function approximating the experimental curve coincides with one of the solutions of the classical sine-Gordon equation, a breather (dynamic soliton), that can be written as follows (Braun and Kivshar, 2004):

$$\psi(x,t) = 4\mathrm{arctg}\left[\left(\frac{\sqrt{1-\omega^2}}{\omega}\right)\frac{\sin(\omega t)}{\mathrm{ch}(x\sqrt{1-\omega^2})}\right], \quad (2)$$

where ω is the inner frequency of the breather, x determines the origin of the curve, and t is the independent variable (time). The approximation error of experimental data is calculated from the formula $\sigma = \sqrt{1/12\sum_{k=1}^{12}(Y_k^E - Y_k^T)^2}$, where $Y_k^E - Y_k^T$ are the residuals between the observed and calculated monthly averaged station positions for the sinusoid and breather. As seen from Table 1 (columns 4 and 5), the approximation of the breather is reducing the σ-value by a factor of two or three as compared to the conventional sinusoidal fitting.

The pattern of measured horizontal displacements shows excellent coincidence with the solution of the sine-Gordon equation for most studied components. This pushed us to apply this equation for developing the model of cyclic components of crustal block movement.

4 The model of periodic crustal block movement

The pattern of the above described changes in the station

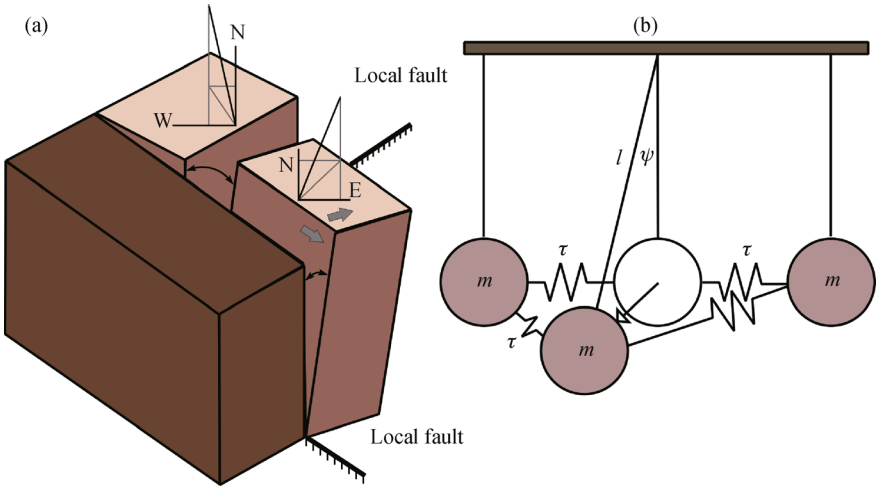

Fig. 4 The generalized model of block movement in the vertical plane along differently oriented local faults of the hinge type due to variable vertical loading. (a) The model of block movement along NE- and NW-striking faults and schemes of the full displacement vector decomposition into components. (b) The model of block movement represented as three coupled identical pendulums (notations are given in the text).

Table 1 The approximation error of experimental data

GPS site	Displacement component	Breather oscillation frequency ω	Approximation error for a breather σ_b	Approximation error for a sinusoid σ_s	The average amplitude of fluctuations in the annual cycle (mm)	Slope $\mathrm{tg}(\psi)_{\max}$	Phase max, min (month of the year; displacement component)	Breather frequency value for the displacement amplitude according to χ^2 criterion
NRGR	"N-S"	0.873	0.048	0.069	9.4	0.36	7 "North"	0.51
	"E-W"	0.780	0.052	0.149	11.1		1 "East"	0.56
					(40.5 Up)			0.85
NRG2	"N-S"	0.8	0.069	0.127	3.57	0.31	5 "North"	0.29
	"E-W"	0.7	0.066	0.222	4.19		1 "West"	0.32
					(17.5 Up)			0.7
TWMS	"N-S"	0.898	0.064	0.149	2.24	0.28	7 "North"	0.23
	"E-W"	0.830	0.110	0.231	2.24		12 "West"	0.23
					(14.53 Up)			0.7
CNPP	"N-S"	0.915	0.074	0.104	3.64	0.28	9 "North"	0.30
	"E-W"	0.919	0.100	0.100	1.69		10 "East"	0.20
	"Up"	0.87	0.062	0.131	15.22		9 "Up"	0.66
FZHS	"N-S"	0.7	0.041	0.168	3.69	0.31	8 "North"	0.30
	"Up"	0.8	0.049	0.081	19.16		8 "Up"	0.72
LJRN	"N-S"	0.79	0.061	0.140	3.11	0.24	11 "North"	0.27
	"Up"	0.85	0.035	0.090	19.05		9 "Up"	0.72
PPBF	"N-S"	0.900	0.041	0.057	3.56	0.36	9 "North"	0.29
	"Up"	0.919	0.045	0.063	14.56		9 "Up"	0.64
MLFP	"N-S"	0.900	0.033	0.113	3.33	0.30	8 "North"	0.28
	"Up"	0.920	0.045	0.102	19.51		9 "Up"	0.73
P106	"N-S"	0.906	0.026	0.029	4.55	0.46	8 "North"	0.34
	"Up"	0.900	0.030	0.050	15.98		9 "Up"	0.67
P716	"N-S"	0.918	0.044	0.061	5.08	0.34	9 "North"	0.36
	"Up"	0.760	0.041	0.135	19.57		9 "Up"	0.73
P566	"N-S"	0.880	0.042	0.094	2.58	0.21	9 "North"	0.24
	"Up"	0.932	0.035	0.031	17.64		9 "Up"	0.70
P725	"N-S"	0.962	0.052	0.078	2.7	0.18	5 "North"	0.25
	"Up"	0.910	0.042	0.055	17.4		7 "Up"	0.69

positions within the annual cycles might be formulated as a problem of block oscillation in the vertical plane. If a block with an adjacent hinge fault (Fig. 4(a)) is considered as a pendulum (Fig. 4(b)), then, in the simplest case, one may choose a physical model of block interaction as a chain of three coupled identical pendulums (Trofimenko and Bykov, 2014).

The equation of motion of the system for the case of a radial force acting on the middle block and deviating it on the angle ψ, can be expressed as

$$I\frac{\partial^2\psi}{\partial t^2} = -mgl\sin\psi + \tau d^2\frac{\partial^2\psi}{\partial x^2}, \quad (3)$$

where I is the moment of inertia of the block, the term $mgl\sin\psi$ is the moment of the gravity force, m is the lumped mass of the pendulum, l is the length of the pendulum (the height of the block), $\tau d^2\frac{\partial^2\psi}{\partial x^2}$ is the sum of the moments of the torsion forces exerted by the adjacent blocks, τ is the constant of the spring torsion (rigidity of the block contact), and d is an increment of the interblock distance (increase or decrease depending on the type of movement). Assuming $\omega^2 = mgl/I$, $c^2 = \tau d^2/I$, and introducing the dimensionless variables $t' = \omega t$ and $x' = x\omega/c$, Eq. (3) is transformed into the sine-Gordon equation (Braun and Kivshar, 2004):

$$\frac{\partial^2\psi}{\partial x'^2} - \frac{\partial^2\psi}{\partial t'^2} = \sin\psi. \quad (4)$$

This equation has a number of analytical solutions, one of which is a breather (dynamic soliton) described by Eq. (2).

5 Discussion of the results

Figure 5 shows a change in the shape of the breather depending on the frequency. One may note that at ω close to 0.9, the shapes of the breather and the sinusoid are practically identical. The asymmetry of the site trajectory shapes appears as frequency decreases. We detected precisely these effects in the displacement curves for the observed GPS stations in the annual cycles (Figs. 2(a)–2(f)). From the Table (column 3) it can be seen that the breather oscillation frequency ω minimizing the fitting error σ_b varies for different GPS sites and displacement components.

In order to test the model developed (3) and verify the identity of the obtained results, we have arbitrarily selected the GPS sites installed under different geological conditions. These include the sites MLFP and PPBF located on either side of the local fault in proximity of the sites TWMS and CNPP (Fig. 1(b)), P566 and P725 located on one side of the local fault (Fig. 1(e)), and P106 and P716

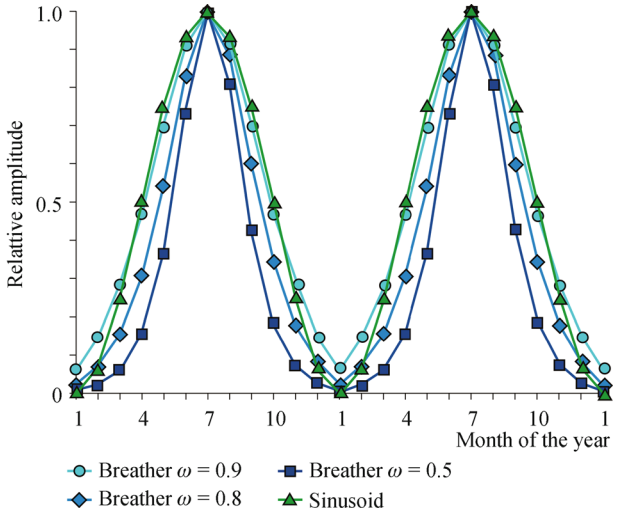

Fig. 5 The sinusoid and breather shapes at different frequencies.

located in tectonically inactive areas of different local fault systems (Fig. 1(f)).

The analysis of the data listed in columns 4 and 5 of the Table shows that for the CNPP site, the shape of the component of the full displacement vector in the annual cycles most optimally corresponds to the sinusoid. The same is true for the separate displacement components at the sites PPBF, P106 (N–S component), P566 (UP component) and P725 (UP component).

For sites MLFP (33.9183° N, 117.3178° W, City Riverside) and PPBF (33.8356° N, 117.1819° W, City Perris), located on either side of the local fault, we obtain the following correlation coefficient values: $k_{NS}(\Delta\varphi = 0) = 0.98$, $k_{EW}(\Delta\varphi = 0) = 0.99$, and $k_{Up}(\Delta\varphi = 0) = 0.98$. As for remote sites P106 (39.4590° N, 112.2623° W, City Leamington) and P716 (44.7183° N, 110.5115° W, Yellowstone National Park), located in different local fault systems, the calculated correlation coefficient values are equal to $k_{NS}(\Delta\varphi = 0) = 0.98$, $k_{EW}(\Delta\varphi = 0) = 0.79$, and $k_{Up}(\Delta\varphi = 0) = 0.95$. The below listed values of the correlation coefficient are obtained for a pair of sites P566 (36.3244° N, 119.2293° W, City Visalia) and P725 (37.0889° N, 119.7456° W, City Coarsegold), located on one side of the local fault: $k_{NS}(\Delta\varphi = 0) = 0.63$, $k_{NS}(\Delta\varphi = 2) = 0.97$, $k_{EW}(\Delta\varphi = 0) = 0.08$, and $k_{EW}(\Delta\varphi = 3) = -0.83$; for the vertical component these values are $k_{Up}(\Delta\varphi = 0) = -0.58$ and $k_{Up}(\Delta\varphi = 4) = 0.99$.

From the obtained results it follows that the local fault location in the approximate vicinity of the sites does not always cause their displacements in adherence to the nonlinear model (3). For example, comparing the displacement curve shapes for the MLFP and PPBF sites, approximated by a breather with a similar frequency, we may conclude that at in-phase displacement of all components, the MLFP site is moving in adherence to solution (2), whereas for the PPBF site, the sinusoidal

approximation function $F(\omega t+\varphi)$ is sufficient (see Eq. (1)). This means that the universal approach for the choice of separate optimal model parameters does not exist because the shape of the site displacement trajectories does not depend on the slope of the block $\mathrm{tg}(\psi)_{\max}$, the maximum values of the displacement amplitudes of the components, or the breather frequency (see columns 7, 6, and 3, respectively, in the Table). The analysis of the shapes of the displacement curves should be started at σ_s values that exceed 0.06 and exhibit a discrepancy between the statistical monthly averaged data and the theoretical sinusoid, as shown in column 5 of the Table.

We can obtain stricter constraints by using Pirson criterion χ^2. To do this, it is sufficient to consider statistical discrepancies between the sinusoid and the breather at different frequency values ω. Let us assume that the site ordinate values for the arbitrary component in the annual cycle correspond to the observed values of the points of the sinusoid $X_i^{\sin}$ ($X_i^{\sin}\in(0,1)$; $i=1, 12$) and a breather-shape curve is the calculated model with the ordinates X_i^{br} ($X_i^{br}\in(0,1)$; $i=1, 12$). If the applied model (3) correctly describes the site displacement in the shape of a sinusoid by the function $F(\omega t+\varphi)$, then the sum of squared deviations $((X_i^{\sin}-X_i^{br})^2$ should not be large (the hypothesis H_0). In our case, to measure the closeness of the observed and expected values we use $\chi^2=C\sum_{i=1}^{12}(X_i^{\sin}-X_i^{br})^2/X_i^{\sin}$, where C is the scale factor assigned for the transformation of the values normalized to the unit interval to really observed maximum displacement amplitudes (shown in column 6 of the Table). The average values of the determination errors for the displacement maxima attain to ±1 mm for the NS and EW components and ±3 mm for the Up component, respectively. A critical value, at which the hypothesis of homogeneity of the studied values is rejected if the number of degrees of freedom $r=k-1=$ 13–1, is equal to 21.026 at 5% significance level ($\alpha=0.05$). As a result of the performed calculations, it has been established that the hypothesis H_0 is rejected at the following ratios of real amplitudes (mm) and breather frequencies (C,ω): (4, 0.3), (7, 0.5), (14, 0.7), (27, 0.8). Column 9 of the Table shows the theoretical frequency values for the real displacement amplitudes of the components. Thus, based on this criterion, the model of nonlinear cyclic displacement of GPS sites (3) can be applicable to sites NRG2 (Up component), FZHS (Up component), and P716 (Up component) (see Table). The suggested model (3) describes the shape of the site displacement curves with less error; however, the discrepancies between the shapes of the curves for the sinusoid and the breather are insignificant and should be taken into consideration only in the case the breather frequency $\omega\leqslant0.7\pm0.05$ with an allowance for the determination errors for the displacement maxima.

6 Conclusions

We have analyzed a set of time series obtained at three pairs of collocated GPS sites situated near the active fault intersection area in the central part of the Stanovoy Range and the southern part of the San Andreas Fault. All the GPS site position time series show notable seasonal variations.

Based on statistical modeling, we have established the applicability criteria for the above considered model of nonlinear displacement of GPS sites (Trofimenko and Bykov, 2014) by performing a qualitative analysis of the shapes of the curves in the annual cycles. Resting upon the representative data, it has been shown that the differences in the displacement trajectories of crustal block movement in the annual cycles are caused by the local fault system, and as typically observed, by the state of the geological medium and its response properties. The regional and global factors stipulate the in-phase variations in the station positions.

Because the meteorological factors in the annual cycles influence the shapes of the movement trajectories of the collocated sites equally (van Dam et al., 1994), the observed phase residuals of the peaks of the site coordinate variations may be linked to periodic displacements along the fault boundaries where the GPS stations have been installed.

The detected high correlation of the observed trajectories of GPS site displacements with one of the solutions of the sine-Gordon equation, a breather, allows us to assume that the mechanism of such oscillations may be related to the appearance of solitary strain waves in the fault intersection system, which in this case, may be qualitatively treated as standing waves of compression-extension of the geological medium (Bykov, 2014).

A simple mathematical model (3) proposed by Trofimenko and Bykov (2014), that describes the oscillations of two interacting blocks, has been successfully applied for modeling fault dynamics, mechanisms of rotation, slippage of crustal blocks, and also, for the interpretation of the observable strain wave effects (Gershenzon et al., 2009; Bykov, 2014). The other possible source of the detected seasonal variations may be irregular in time deformations of the fault zones due to their different types of rheology.

After examination of periodic displacements in the annual cycles of GPS sites located in close proximity to active faults, different types of displacements have been established for the considered pairs of sites. These include in-phase and anti-phase changes of the components of the full displacement vector, the relative time delay of the maxima and minima for separate components, and the dissimilarities of the displacement trajectory from the sinusoid. The causes of these dissimilarities can be related only to the local rheology of the fault zones and tectonic stress transfer (migrating of crustal deformation in the form of slow strain waves).

Acknowledgements This study was partly funded through the state task No. 5.1771.2014/K of the Ministry of Education and Science of the Russian Federation and by the Russian Foundation for Basic Research (RFBR) according to the research project No.16-05-00097a and by the Far Eastern Federal University, project No. 14-08-01-05_m.

References

Altamimi Z, Collilieux X, Legrand J, Garayt B, Boucher C (2007). ITRF2005: a new release of the International Terrestrial Reference Frame based on time series of station positions and Earth Orientation Parameters. J Geophys Res, 112(B9): B09401

Blewitt G, Lavallee D, Clarke P, Nurutdinov K (2001). A new global mode of Earth deformation: seasonal cycle detected. Science, 294 (5550): 2342–2345

Braun O M, Kivshar Y S (2004). The Frenkel-Kontorova Model: Concepts, Methods, and Applications. Berlin: Springer

Bykov V G (2014). Sine-Gordon equation and its application to tectonic stress transfer. J Seismol, 18(3): 497–510

Chen Q, van Dam T, Sneeuw N, Collilieux X, Weigelt M, Rebischung P (2013). Singular spectrum analysis for modeling seasonal signals from GPS time series. J Geodyn, 72: 25–35

Gershenzon N I, Bykov V G, Bambakidis G (2009). Strain waves, earthquakes, slow earthquakes, and afterslip in the framework of the Frenkel-Kontorova model. Physical Review E, 79: 056601

GPS explorer portal. http://geoapp03.ucsd.edu/gridsphere/gridsphere?cid = Select + Sites

Herring T A, King R W, McClusky S C (2010). Reference manual GAMIT. GPS analysis at MIT release 10.4, Department of Earth, Atmospheric, and Planetary Sciences Massachusetts Institute of Technology, http://chandler.mit.edu/~simon/gtgk/GAMIT_Ref_10.4.pdf

Serpelloni E, Faccenna C, Spada G, Dong D, Williams S D P (2013). Vertical GPS ground motion rates in the Euro-Mediterranean region: new evidence of velocity gradients at different spatial scales along the Nubia-Eurasia plate boundary. J Geophys Res, 118(11): 6003–6024

Shestakov N, Takahashi H, Ohzono M, Prytkov A, Bykov V, Gerasimenko M, Luneva M, Gerasimov G, Kolomiets A, Bormotov V, Vasilenko N, Baek J, Park P H, Serov M (2012). Analysis of the far-field crustal displacements caused by the 2011 Great Tohoku earthquake inferred from continuous GPS observations. Tectonophysics, 524–525: 76–86

Trofimenko S V, Bykov V G (2014). The model of crustal block movement in the South Yakutia geodynamic testing area based on GPS data. Russ J Pac Geol, 8(4): 247–255

van Dam T M, Blewitt G, Heflin M B (1994). Atmospheric pressure loading effects on global positioning system coordinate determinations. J Geophys Res, 99(B12): 23939–23950